

## Predicting the Rossby number in convective experiments

EVAN H. ANDERS,<sup>1,2</sup> CATHRYN M. MANDUCA,<sup>2</sup> BENJAMIN P. BROWN,<sup>1,2</sup> JEFFREY S. OISHI,<sup>3</sup> AND GEOFFREY M. VASIL<sup>4</sup>

<sup>1</sup>*Dept. Astrophysical & Planetary Sciences, University of Colorado – Boulder, Boulder, CO 80309, USA*

<sup>2</sup>*Laboratory for Atmospheric and Space Physics, Boulder, CO 80303, USA*

<sup>3</sup>*Department of Physics and Astronomy, Bates College, Lewiston, ME 04240, USA*

<sup>4</sup>*University of Sydney School of Mathematics and Statistics, Sydney, NSW 2006, Australia*

(Received October 18, 2018; Revised ??; Accepted ??)

Submitted to ApJL

### ABSTRACT

The Rossby number is a crucial parameter describing the degree of rotational constraint on the convective dynamics in stars and planets. However, it is not an input to computational models of convection but must be measured ex post facto. Here, we report the discovery of a new quantity, the Predictive Rossby number, which is both tightly correlated with the Rossby number and specified in terms of common inputs to numerical models. The Predictive Rossby number can be specified independent of Rayleigh number, allowing suites of numerical solutions to separate the degree of rotational constraint from the strength of the driving of convection. We examine the scaling of convective transport in terms of the Nusselt number and the degree of turbulence in terms of the Reynolds number of the flow. Finally, we describe the boundary layers as a function of increasing turbulence at constant Rossby number.

*Keywords:* convection — rotation — turbulence

### 1. INTRODUCTION

Rotation influences the dynamics of convective flows in stellar and planetary atmospheres. Many studies on the fundamental nature of rotating convection in both laboratory and numerical settings have provided great insight into the properties of convection in both the rapidly rotating regime (Julien et al. 2012; Stellmach et al. 2014; Gastine et al. 2016) and the transition to the rotationally unconstrained regime (King et al. 2009; Zhong et al. 2009; Cheng et al. 2015). The scaling behavior of heat transport, the nature of convective flow structures, and the importance of boundary layer-bulk interactions in driving dynamics are well known. Yet, we do not know of any simple procedure for predicting the magnitude of vortical flow gradients purely from experimental control parameters, such as bulk rotation rate and thermal input.

In the astrophysical context, many studies of rotating convection have investigated questions inspired by the solar dynamo (Glatzmaier & Gilman 1982; Busse 2002; Brown et al. 2008, 2010, 2011; Augustson et al. 2012; Guerrero et al. 2013; Käpylä et al. 2014). Even when these simulations nominally rotate at the solar rate, they frequently produce distinctly different behaviors than the true Sun, such as anti-solar differential rotation profiles (Gastine et al. 2014). It seems that these differences occur because the simulations produce less rotationally constrained states than the Sun. The influence of rotation results from the local shear gradients, and these are not direct input parameters. Recent simulations predict significant rotational influence in the deep solar interior, which can drastically affect flows throughout the solar convection zone (Featherstone & Hindman 2016; Greer et al. 2016). In the planetary context, the balance between magnetic and rotational forces likely leads to the observed differences between ice giant and gas giant dynamos in our solar system (Soderlund et al. 2015). In particular, Aurnou & King (2017) suggest that many studies of planetary systems have over-emphasized the importance of magnetism compared to rotation.

In short, simulations must achieve the proper rotational balance if they are to explain the behavior of astrophysical objects. The degree of rotational influence is best assessed by the ratio between nonlinear advection magnitude, and the linear Coriolis accelerations. The *Rossby number* is the standard measure of this ratio,

$$\text{Ro} \equiv \frac{|\nabla \times \mathbf{u}|}{2|\mathbf{\Omega}|} \sim \frac{|(\nabla \times \mathbf{u}) \times \mathbf{u}|}{|2\mathbf{\Omega} \times \mathbf{u}|}, \quad (1)$$

where  $\mathbf{\Omega}$  denotes the bulk rotation vector. Many proxies for the dynamical Rossby number exist that are based solely on input parameters, most notably the *convective* Rossby number. However, all proxies produce imperfect predictions for the true dynamically relevant quantity.

*In this letter, we demonstrate an empirical method of predicting the output Rossby number of convection in a simple stratified system.*

In Anders & Brown (2017) (hereafter AB17), we studied non-rotating compressible convection without magnetic fields in polytropic atmospheres. In this work, we extend AB17 to rotationally-influenced, *f*-plane atmospheres (e.g. Brummell et al. 1996, 1998; Calkins et al. 2015). We determine how the input parameters we studied previously, controlling the Mach and Reynolds numbers of the evolved flows, couple with the Taylor number (Ta, Julien et al. 1996), which sets the magnitude of the rotational vector.

In section 2, we describe our experiment and paths through parameter space. In section 3, we present the results of our experiments and in section 4 we offer concluding remarks.

## 2. EXPERIMENT

We study fully compressible, stratified convection under precisely the same atmospheric model as in AB17, but here we have included rotation. We study polytropic atmospheres with  $n_\rho = 3$  density scale heights and a superadiabatic excess of  $\epsilon = 10^{-4}$  such that flows are at low Mach number. We study a domain in which the gravity,  $\mathbf{g} = -g\hat{z}$ , and rotational vector,  $\mathbf{\Omega} = \Omega\hat{z}$ , are antiparallel (as in e.g., Julien et al. 1996; Brummell et al. 1996).

We evolve the velocity ( $\mathbf{u}$ ), temperature ( $T$ ), and log density ( $\ln \rho$ ) according to the Fully Compressible Navier-Stokes equations in the same form presented in AB17, with the addition of the Coriolis term,  $2\mathbf{\Omega} \times \mathbf{u}$ , to the left-hand side of the momentum equation. We impose impenetrable, stress-free, fixed-temperature boundary conditions at the top and bottom of the domain.

We set the kinematic viscosity ( $\nu$ ), thermal diffusivity ( $\chi$ ), and strength of rotation ( $\Omega$ ) at the top of the domain by choosing the Rayleigh number (Ra), Prandtl number (Pr), and Taylor number (Ta),

$$\text{Ra} = \frac{gL_z^3 \Delta S / c_P}{\nu \chi}, \quad \text{Pr} = \frac{\nu}{\chi}, \quad \text{Ta} = \left( \frac{2\Omega L_z^2}{\nu} \right)^2, \quad (2)$$

where  $L_z$  is the depth of the domain as defined in AB17,  $\Delta S \propto \epsilon n_\rho$  is the specific entropy difference between  $z = 0$  and  $z = L_z$ , and the specific heat at constant pressure is  $c_P = \gamma/(\gamma - 1)$  and  $\gamma = 5/3$ . Throughout this work we set  $\text{Pr} = 1$ . The Taylor number relates to the often-quoted Ekman by the equality  $\text{Ek} \equiv \text{Ta}^{-1/2}$ .

The *convective* Rossby number has provided (e.g., Julien et al. 1996; Brummell et al. 1996) a common proxy (based on input parameters) for the degree of rotational constraint,

$$\text{Ro}_c = \sqrt{\frac{\text{Ra}}{\text{Pr Ta}}} = \frac{1}{2\Omega} \sqrt{\frac{g \Delta S}{c_P L_z}}. \quad (3)$$

This parameter measures the importance of buoyancy relative to rotation without involving dissipation. We show that true Rossby number defined in equation 1 depends nonlinearly on  $\text{Ro}_c$ .

The wavenumber of convective onset increases such that,  $k_{\text{crit}} \propto \text{Ta}^{1/6}$  (Chandrasekhar 1961; Calkins et al. 2015). We study horizontally-periodic, 3D Cartesian convective domains with extents of  $x, y = [0, 4(2\pi/k_{\text{crit}})]$  and  $z = [0, L_z]$ . At large values of Ta, these domains are tall and skinny, as in Stellmach et al. (2014). We evolve our simulations using the Dedalus<sup>1</sup> pseudospectral framework, and our numerical methods are identical to those presented in AB17.

The critical value of Ra at which convection onsets also depends on Ta (see the black line in figure 1a); roughly according to  $\text{Ra}_{\text{crit}} \sim \text{Ta}^{2/3}$  (Chandrasekhar 1961; Calkins et al. 2015). We have confirmed these scalings of  $\text{Ra}_{\text{crit}}(\text{Ta})$  and  $k_{\text{crit}}(\text{Ta})$  in our atmospheres using a linear stability analysis. Even taking account of linear theory, the dependence of the evolved nonlinear fluid flows on the input parameters makes predicting the rotational constraint very challenging. We will explore three paths through Ra-Ta space:

$$\text{Ra} = \begin{cases} S \text{Ra}_{\text{crit}}(\text{Ta}), & \text{(I)} \\ (\text{Ro}_c)^2 \text{Pr Ta}, & \text{(II)} \\ (\text{Ro}_p)^2 \text{Pr Ta}^{3/4} & \text{(III)}. \end{cases} \quad (4)$$

Paths on constraint I are at constant supercriticality,  $S \equiv \text{Ra}/\text{Ra}_{\text{crit}}$  (blue dash-dot line in figure 1a). Paths

<sup>1</sup> <http://dedalus-project.org/>

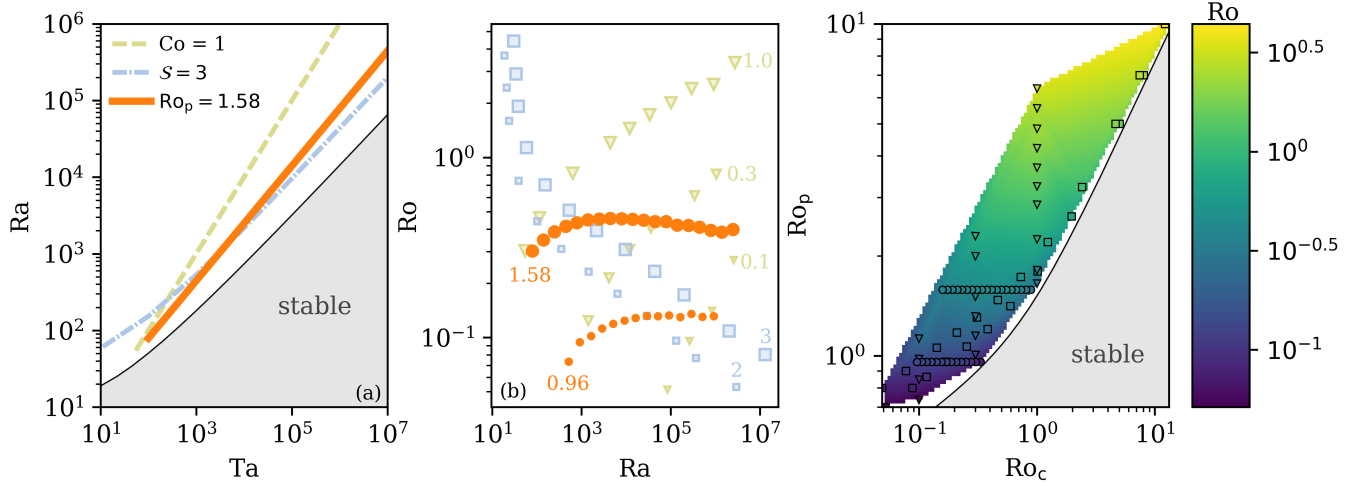


**Figure 1.** (a) The critical Rayleigh number, as a function of the Taylor number, is plotted as a solid black line. The grey shaded region is subcritical, and rotation suppresses convection there. Paths of constant Convective Rossby Number ( $Ro_c$ , green dashed line), constant supercriticality ( $\mathcal{S}$ , blue dash-dot line), and constant  $Ro_p$  (orange solid line) are shown through parameter space. (b) Evolved  $Ro$  is plotted vs.  $Ra$  along paths of  $Ro_p = [1.58, 0.96]$  for [big, small] orange circles. For comparison, paths of constant  $\mathcal{S}$  (blue squares,  $\mathcal{S} = [3, 2]$  for [big, small] squares) and constant  $Ro_c$  (green triangles,  $Ro_c = [1, 0.3, 0.1]$  for [big, medium, small] triangles) are shown.  $Ro$  is roughly constant for a constant  $Ro_p$ , particularly for the low- $Ro$ ,  $Ro_p = 0.96$  case, but changes drastically at constant  $Ro_c$  or  $\mathcal{S}$ . (c) The evolved value of  $Ro$  is shown as a function of  $Ro_p$  and  $Ro_c$ . Each of the experiments in (b) is outlined by a black (circle, triangle, square) for points along constant ( $Ro_p$ ,  $Ro_c$ ,  $\mathcal{S}$ ) paths. The color inside of the marker represents the exact measured  $Ro$  of that experiment, while the colormap outside of markers is a linear interpolation of the data set. A least-squares fit to all experiments with  $\mathcal{S} \geq 1.5$  and  $Ro \geq 0.3$  returns  $Ro = 0.2Ro_c^{-0.19}Ro_p^{1.5}$ . A similar fit to all experiments with  $\mathcal{S} \geq 1.5$  and  $Ro < 0.3$  returns  $Ro = 0.1Ro_c^{-0.21}Ro_p^{3.5}$ . In both the high- and low-  $Ro$  regime, the measured Rossby number is a strong function of  $Ro_p$  and a weak function of  $Ro_c$ .

on constraint II are at a constant value of the classic  $Ro_c$  (green dashed line in figure 1a). Paths on constraint III (e.g., orange solid line in figure 1a) set constant a ratio which we call the “Predictive Rossby Number,”

$$Ro_p = \sqrt{\frac{Ra}{Pr Ta^{3/4}}} = \frac{1}{2\Omega} \sqrt{\frac{g \Delta S}{c_p L_p}} \quad (5)$$

To our knowledge, these paths have not been reported in the literature. The importance of the predictive Rossby number implies the importance of a dynamical length scale,

$$L_p \sim \frac{L_z}{Ta^{1/4}} \quad (6)$$

This differs noticeably from the anticipated onset length scale

$$L_{crit.} \sim \frac{L_z}{Ta^{1/6}}. \quad (7)$$

Length-scale corrections of the form of equation 6 have been proposed in systems with no-slip boundary conditions and Ekman pumping effects. However, we see this scale in a system with stress-free boundaries and ostensibly no significant Ekman fluxes.

### 3. RESULTS

In figure 1a, the value of  $Ra_{crit}$  is shown as a function of  $Ta$ , as calculated by a linear instability analysis. A sample path for each criterion in equation 4 through this parameter space is shown. In figure 1b, we display the evolution of  $Ro$  with increasing  $Ra$  along various paths through parameter space. We find that  $Ro$  increases on constant  $Ro_c$  paths, decreases on constant  $\mathcal{S}$  paths, and remains roughly constant along constant  $Ro_p$  paths. In figure 1c, the value of  $Ro$  is shown simultaneously as a function of  $Ro_p$  and  $Ro_c$  for all experiments conducted in this study. We find a general power-law of the form  $Ro \propto Ro_c^{-1/5} Ro_p^\alpha$ , where  $\alpha \approx 3.5$  in the rotationally constrained, low- $Ro$  regime and  $\alpha \approx 1.5$  in the unconstrained, high- $Ro$  regime. In the rotationally constrained regime,  $Ro$  is a much stronger function of  $Ro_p$  than  $Ro_c$ , and the evolved  $Ro$  can be approximately determined through specification of  $Ro_p$  alone.

In figure 2, sample snapshots of the evolved entropy field in the  $x$ - $y$  plane near the top of the domain are shown. In the left panel is a rotationally unconstrained flow at moderately high  $Ro$ , and  $Ro$  decreases into the rotationally constrained regime from left to right. As  $Ro$  decreases, the classic granular structure of convection (see e.g., figure 2 in AB17) gives way to vortical columns of convection, as seen in rapidly rotating Rayleigh-

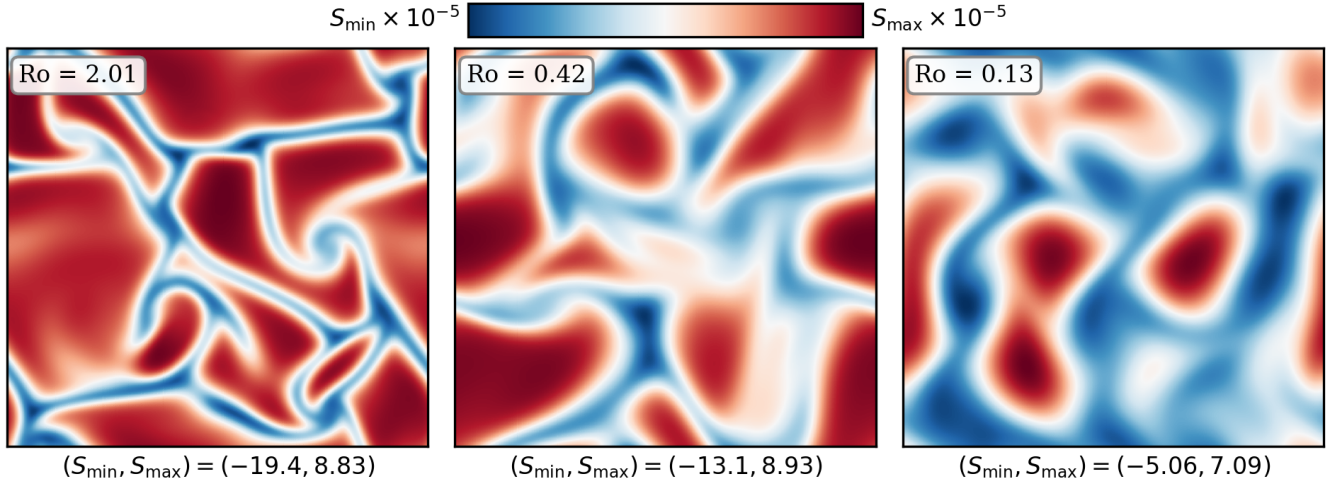


**Figure 2.** A horizontal slice of the evolved entropy field is plotted at  $z = 0.95L_z$  for select simulations. The mean value of entropy at this height has been removed in all cases. All runs displayed here have an evolved volume-averaged  $Re \approx 200$ . As  $Ro$  decreases from  $O(1)$  on the left to  $O(0.1)$  on the right, and thus the rotational constraint on the flow increases, significant changes in flow morphology are observed. At  $Ro = 2.01$  ( $Ro_c = 1$ ), convective dynamics are not hugely dissimilar from the non-rotating case where there are large upflows and narrow, fast downflow lanes (see e.g., AB17). As the rotational constraint increases, the granular convective pattern gives way to vortical columns, as seen at  $Ro = 0.13$  ( $Ro_p = 0.96$ ).

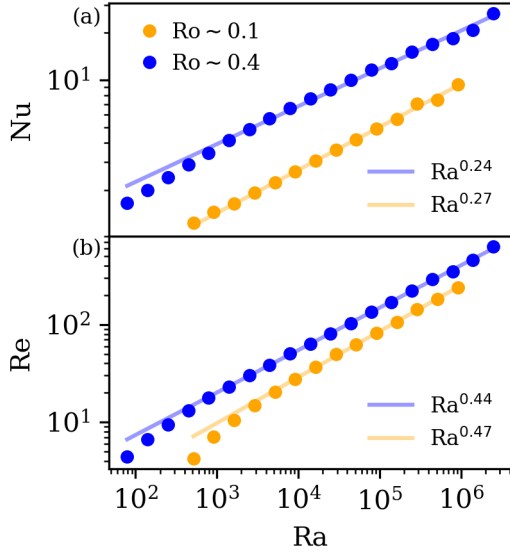


**Figure 3.** Scaling laws for paths at  $Ro_p = 1.58$  ( $Ro \approx 0.4$ ) and  $Ro_p = 0.96$  ( $Ro \approx 0.1$ ) are shown. (a) Evolved  $Nu$  vs.  $Ra$ . The scaling laws here are very reminiscent of classic Rayleigh-Bénard convection theory (Ahlers et al. 2009). (b) Evolved  $Re$  vs.  $Ra$ . The scaling seen here is nearly identical to scalings in nonrotating convection.

Bénard convection (Stellmach et al. 2014). The select cases displayed in figure 2 each have an evolved volume-averaged  $Re \approx 200$ .

We measure the Nusselt number ( $Nu$ ), which quantifies heat transport in a convective solution, as defined in AB17. In figure 3a, we show how  $Nu$  scales as a function

of  $Ra$  at fixed  $Ro_p$ . When  $Ro \sim 0.1$ , we find a scaling of  $Nu \propto Ra^{0.27}$ . This is reminiscent of classic scaling laws (e.g.,  $Ra^{2/7}$ ) in non-rotating Rayleigh-Bénard convection (Ahlers et al. 2009). This suggests that changes in heat transport at constant  $Ro_p$  are driven by changes in the thermal boundary layer structure with increasing  $Ra$ . In figure 3b, we plot the RMS Reynolds number ( $Re = |u|L_z/\nu$ ) as a function of  $Ra$  at fixed  $Ro_p$ , and find that  $Re \propto Ra^{0.47}$  in the rotationally constrained regime, which is almost precisely the  $Re \propto Ra^{1/2}$  scaling measured in the non-rotating regime in AB17.

Figure 4 shows time- and horizontally-averaged profiles of  $Ro$  and the  $z$ -component of the specific entropy gradient,  $\partial_z s$ . Figures 4a&b show these profiles for  $Ro_p = 0.96$  ( $Ro \approx 0.1$ ), while Figures 4c&d show these profiles for  $Ro_p = 1.58$  ( $Ro \approx 0.4$ ). The transition in profile behavior from low  $Ra$  (yellow) to high  $Ra$  (purple) is denoted by the color of the profile. As  $Ra$  increases at a constant value of  $Ro_p$ , both the thermal ( $\partial_z s$ ) and dynamical ( $Ro$ ) boundary layers become thinner. We measure the thickness of the thermal boundary layer ( $\delta_s$ ) at the top of the domain by measuring where a linear fit within the boundary layer crosses through  $\partial_z s = 0$ . We ensure by-eye for each profile that this is a reasonable measure of the boundary layer thickness. We measure the thickness of the  $Ro$  boundary layer ( $\delta_{Ro}$ ) as the height of the peak value of  $Ro$  within the upper half of the domain. In figure 4e, we plot  $\delta_{Ro}/\delta_s$ , the ratio of the sizes of these two boundary layers. As anticipated, the dynamical boundary layer ( $\delta_{Ro}$ ) becomes relatively



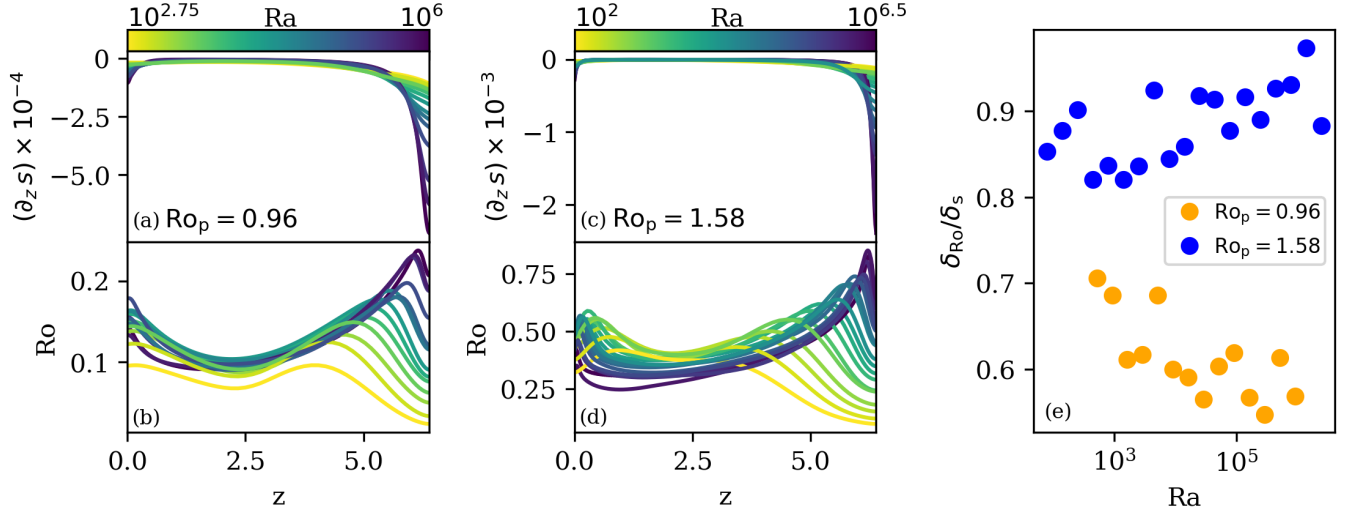


**Figure 4.** Horizontally-averaged profiles of the  $z$ -derivative of the specific entropy profile ( $\partial_z s$ , a) and Rossby number ( $Ro$ , b) are shown vs. height for  $Ro_p = 0.96$  ( $Ro \approx 0.1$ ). Similar profiles are shown in (c) and (d) for  $Ro_p = 1.58$  ( $Ro \approx 0.4$ ). The color of the profiles denotes the value of  $Ra$ , with yellow profiles being at very low  $Ra$  and purple at the highest values of  $Ra$  studied here. (e) The ratio of the thicknesses of the dynamical ( $Ro$ ) boundary layers and thermal ( $\partial_z s$ ) boundary layers is shown for both values of  $Ro_p$  at each value of  $Ra$ . This ratio, and thus the relative importance of both thermal and rotational dynamics, remains roughly constant across orders of magnitude of  $Ra$ .

thinner with respect to the thermal boundary layer ( $\delta_s$ ) as  $Ro$  and  $Ro_p$  decrease. At  $Ro_p = 1.58$ , both boundary layers are approximately equally thick, and so both rotational and advective effects are equally important. On the other hand, at  $Ro_p = 0.96$ , the dynamical boundary layer is half the size of the thermal boundary layer, and rotational effects dominate the dynamics.

#### 4. DISCUSSION

In this letter, we studied low-Mach-number, stratified, compressible convection under the influence of rotation. We examined three paths through  $Ra$ - $Ta$  space, and showed that in the rotationally constrained regime at low- $Ro$ , the newly-defined Predictive Rossby number,  $Ro_p = Ra/(Pr Ta^{3/4})$ , determines the value of the evolved  $Ro$ . While increasing  $Ra$  and holding  $Ro_p$  constant, we find scaling laws of heat transport ( $Nu$ ) and turbulence ( $Re$ ) that are nearly identical to scaling laws seen in nonrotational convection. We note briefly that the scaling  $Ra \propto Ta^{3/4}$  is very similar to the theorized boundary between fully rotationally constrained convection and partially constrained convection predicted in Boussinesq theory, of  $Ra \propto Ta^{4/5}$  (Julien et al. 2012; Gastine et al. 2016). This  $Ta^{4/5}$  scaling arises through arguments of geostrophic balance in the boundary layers, and is a steeper scaling than the  $Ta^{3/4}$  scaling

present in  $Ro_p$ . This suggests that at sufficiently low  $Ro_p$ , a suite of simulations across many orders of magnitude of  $Ra$  will not only have the same volume-averaged value of  $Ro$  (as in Fig. 1b), but will also maintain proper force balances within the boundary layers.

Our results suggest that by choosing the proper value of  $Ro_p$ , experimenters can select the degree of rotational constraint present in their simulations. Once that value is chosen, it is straightforward to increase the turbulent nature of the simulations by increasing  $Ra$ , just as in the non-rotating case. Although all the results reported here are for a simple Cartesian geometry with antiparallel gravity and rotation, preliminary 3D spherical simulations suggest that  $Ro_p$  also specifies  $Ro$  in more complex geometries (Brown et al. 2019 in prep).

This work was supported by NASA Headquarters under the NASA Earth and Space Science Fellowship Program – Grant 80NSSC18K1199. EHA further acknowledges the University of Colorado’s George Ellery Hale Graduate Student Fellowship. This work was additionally supported by NASA LWS grant number NNX16AC92G. Computations were conducted with support by the NASA High End Computing (HEC) Program through the NASA Advanced Supercomputing (NAS) Division at Ames Research Center on Pleiades with allocation GID s1647.

#### REFERENCES

- Ahlers, G., Grossmann, S., & Lohse, D. 2009, *Rev. Mod. Phys.*, 81, 503
- Anders, E. H., & Brown, B. P. 2017, *Physical Review Fluids*, 2, 083501
- Augustson, K. C., Brown, B. P., Brun, A. S., Miesch, M. S., & Toomre, J. 2012, *ApJ*, 756, 169
- Aurnou, J. M., & King, E. M. 2017, *Proceedings of the Royal Society of London Series A*, 473, 20160731
- Brown, B. P., Browning, M. K., Brun, A. S., Miesch, M. S., & Toomre, J. 2008, *ApJ*, 689, 1354
- . 2010, *ApJ*, 711, 424
- Brown, B. P., Miesch, M. S., Browning, M. K., Brun, A. S., & Toomre, J. 2011, *ApJ*, 731, 69
- Brummell, N. H., Hurlburt, N. E., & Toomre, J. 1996, *ApJ*, 473, 494
- . 1998, *ApJ*, 493, 955
- Busse, F. H. 2002, *Physics of Fluids*, 14, 1301
- Calkins, M. A., Julien, K., & Marti, P. 2015, *Geophysical and Astrophysical Fluid Dynamics*, 109, 422
- Chandrasekhar, S. 1961, *Hydrodynamic and hydromagnetic stability*
- Cheng, J. S., Stellmach, S., Ribeiro, A., et al. 2015, *Geophysical Journal International*, 201, 1
- Featherstone, N. A., & Hindman, B. W. 2016, *ApJ*, 830, L15
- Gastine, T., Wicht, J., & Aubert, J. 2016, *Journal of Fluid Mechanics*, 808, 690
- Gastine, T., Yadav, R. K., Morin, J., Reiners, A., & Wicht, J. 2014, *MNRAS*, 438, L76
- Glatzmaier, G. A., & Gilman, P. A. 1982, *ApJ*, 256, 316
- Greer, B. J., Hindman, B. W., & Toomre, J. 2016, *ApJ*, 824, 4
- Guerrero, G., Smolarkiewicz, P. K., Kosovichev, A. G., & Mansour, N. N. 2013, *ApJ*, 779, 176
- Julien, K., Knobloch, E., Rubio, A. M., & Vasil, G. M. 2012, *Physical Review Letters*, 109, 254503
- Julien, K., Legg, S., McWilliams, J., & Werne, J. 1996, *Journal of Fluid Mechanics*, 322, 243
- Käpylä, P. J., Käpylä, M. J., & Brandenburg, A. 2014, *A&A*, 570, A43
- King, E. M., Stellmach, S., Noir, J., Hansen, U., & Aurnou, J. M. 2009, *Nature*, 457, 301
- Soderlund, K. M., Sheyko, A., King, E. M., & Aurnou, J. M. 2015, *Progress in Earth and Planetary Science*, 2, 24
- Stellmach, S., Lischper, M., Julien, K., et al. 2014, *PhRvL*, 113, 254501
- Zhong, J.-Q., Stevens, R. J. A. M., Clercx, H. J. H., et al. 2009, *Physical Review Letters*, 102, 044502